

Surface Electronic Structure Engineering of Manganese Bismuth Tellurides Guided by Micro-Focused Angle-Resolved Photoemission

Klara Volckaert, Paulina Majchrzak, Deepnarayan Biswas, Alfred J. H. Jones, Marco Bianchi, Zhihao Jiang, Raphaël Dubourg, Rasmus Ørnekoll Stenshøj, Mads Lykke Jensen, Nykola C. Jones, Søren V. Hoffmann, Jian-Li Mi, Martin Bremholm, Xing-Chen Pan, Yong P. Chen, Philip Hofmann, Jill A. Miwa, and Søren Ulstrup*

Modification of the electronic structure of quantum matter by ad atom deposition allows for directed fundamental design of electronic and magnetic properties. This concept is utilized in the present study in order to tune the surface electronic structure of magnetic topological insulators based on MnBi_2Te_4 . The topological bands of these systems are typically strongly electron-doped and hybridized with a manifold of surface states that place the salient topological states out of reach of electron transport and practical applications. In this study, micro-focused angle-resolved photoemission spectroscopy (microARPES) provides direct access to the termination-dependent dispersion of MnBi_2Te_4 and MnBi_4Te_7 during in situ deposition of rubidium atoms. The resulting band structure changes are found to be highly complex, encompassing coverage-dependent ambipolar doping effects, removal of surface state hybridization, and the collapse of a surface state band gap. In addition, doping-dependent band bending is found to give rise to tunable quantum well states. This wide range of observed electronic structure modifications can provide new ways to exploit the topological states and the rich surface electronic structures of manganese bismuth tellurides.

as extremely attractive designer quantum materials with potential applications in spintronics and topotronics.^[1–3] Their magnetic, electronic, optical, and topological properties can be widely tuned by various mechanisms of doping,^[4–7] layered synthesis,^[2,8–10] and optical excitation.^[11–14] The parent compound in this family of materials is MnBi_2Te_4 , which consists of ferromagnetic Te-Bi-Te-Mn-Te-Bi-Te septuple layers. In bulk crystals of MnBi_2Te_4 , the interlayer exchange interaction establishes an antiferromagnetic ground state.^[15] Stacking of alternating magnetic MnBi_2Te_4 and non-magnetic Bi_2Te_3 layers leads to magnetically tunable van der Waals heterostructures with the chemical formula $\text{MnBi}_2\text{Te}_4(\text{Bi}_2\text{Te}_3)_m$, where m is a positive integer. By increasing the number of Bi_2Te_3 spacer layers the interlayer exchange interaction is reduced, which can cause a spin-flop transition to a ferromagnetic state.^[8,16–19]


1. Introduction

Intrinsic magnetic topological insulators based on manganese bismuth tellurides (MBTs) have come to prominence

These salient features of the MBT systems have led to the realization of the quantum anomalous Hall effect at temperatures ranging from 1.4 to 7.0 K,^[5,20,21] as well as exotic axion and Chern insulator states.^[22]

K. Volckaert, P. Majchrzak, D. Biswas, A. J. H. Jones, M. Bianchi, Z. Jiang, R. Dubourg, R. Ø. Stenshøj, M. L. Jensen, N. C. Jones, S. V. Hoffmann, Y. P. Chen, P. Hofmann, J. A. Miwa, S. Ulstrup
Department of Physics and Astronomy
Interdisciplinary Nanoscience Center, Aarhus University
Aarhus C 8000, Denmark
E-mail: ulstrup@phys.au.dk

J.-L. Mi, M. Bremholm
Department of Chemistry
Interdisciplinary Nanoscience Center, Aarhus University
Aarhus C 8000, Denmark
X.-C. Pan, Y. P. Chen
Advanced Institute for Materials Research
Tohoku University
Sendai 980-8577, Japan
Y. P. Chen
Department of Physics and Astronomy and School of Electrical and Computer Engineering and Purdue Quantum Science and Engineering Institute
Purdue University
West Lafayette, IN 47907, USA

 The ORCID identification number(s) for the author(s) of this article can be found under <https://doi.org/10.1002/adma.202301907>

© 2023 The Authors. Advanced Materials published by Wiley-VCH GmbH. This is an open access article under the terms of the Creative Commons Attribution License, which permits use, distribution and reproduction in any medium, provided the original work is properly cited.

DOI: 10.1002/adma.202301907

MBTs tend to cleave with microscopic domains of different surface terminations that are characterized by extremely rich surface electronic structures. Their energy- and momentum-dependent dispersion relations have been resolved by angle-resolved photoemission spectroscopy (ARPES) with micro-focused laser systems operating with photon energies below 7 eV, enabling observation of hybridized surface bands and Rashba effects that are intertwined with topological states.^[1,2,12,23–28] The measurements also reveal that the as-grown materials are strongly electron-doped, most likely due to interstitial defects that lead to a deficit of Mn atoms.^[29] The doping typically places the topological bands at binding energies in the range between 200–300 meV, making it practically challenging to achieve electron transport via the topological state. It is therefore highly desirable to further develop platforms for tuning the chemical potential and surface electronic structure of MBTs while being able to probe the effects of such modifications in situ by micro-focused ARPES (microARPES).

Substitution at the Bi sites of MBT crystals with Sb has been demonstrated as a viable method for shifting the chemical potential over a range of 400 meV between the bulk valence band (BVB) and the bulk conduction band (BCB) while maintaining the salient magnetic properties of MnBi_2Te_4 .^[4] Applying a similar strategy for the $m = 1$ heterostructure, i.e. MnBi_4Te_7 , leads to more complex behaviors, as the Sb substitution alters the magnetic properties by making the ferromagnetic ground state more favorable than the antiferromagnetic, which is interesting in its own merit for tuning and inducing Weyl fermions or axion insulators.^[30–34] A downside of Sb substitution is that the doping cannot be monitored in situ but requires synthesis of multiple different crystals, leading to large sample variability between different experiments.^[35]

An alternative strategy that solves this problem is based on dosing alkali metals, such as Li, K, Rb, or Cs, on the material surface while collecting ARPES spectra, which has been demonstrated on a range of semimetals^[36–38] and semiconductors.^[39–42] In the simplest approximation, the adsorbed alkali metals provide electron doping at the surface of the materials with the effect of merely shifting the chemical potential. This picture has proven much too simple in a recent study of alkali-driven electronic structure modifications of MnBi_2Te_4 bulk and thin films, where surprising hole doping effects were observed.^[7,10] The impact of alkali adsorption on the various possible surface terminations of MBT heterostructure compounds has not been investigated and a universal picture of the effect of alkali doping on the MBT family of materials is lacking. Such doping-dependent ARPES studies are complicated by the fact that surface adsorption strongly affects the surface potential of the materials, which in turn impacts the ARPES photoemission intensity through photon energy-dependent matrix element effects. It is therefore beneficial to employ photon-energy tunable sources in the extreme ultraviolet range that are complementary to the low-energy laser-based ARPES methods. Moreover, it is crucial to apply a micro-focused beam for ARPES to permit spatially distinguishing different surface terminations.

2. Results and Discussion

This study presents a systematic approach for tuning the surface electronic structure of MBTs following the outline in **Figure 1a**.

In situ Rb deposition on the surfaces of bulk crystals of the basic building blocks MnBi_2Te_4 and Bi_2Te_3 as well as the two possible surface terminations of MnBi_4Te_7 is tracked by ARPES with microscale spatial resolution at the new SGM4 beamline for micro- and nanoARPES at the ASTRID2 light source, Aarhus University.^[43] Photons with tunable energy over a range of 14–150 eV are obtained from an undulator insertion device and selected using a spherical grating monochromator (SGM-type). An intermediate beam focus with a diameter on the order of 60 μm is achieved using two separate plane ellipse mirrors placed after the monochromator. The beam is then demagnified on a capillary optic [Sigray Inc.], which is placed approximately 7.8 mm from the sample surface. The capillary produces a minimum lateral spot-size with a diameter of 3.1 μm on the sample, as determined from knife edge measurements. The optic is achromatic and highly transmissive as it operates essentially as an elliptical mirror, enabling photon energy-tunable microARPES over the full energy range of the beamline. Photoemitted electrons from the microscopic spot on the sample are collected using a SPECS Phoibos 150 scanning angle lens (SAL) analyzer, such that angle-resolved spectra can be measured both parallel and perpendicular to the analyzer slit without sample rotation. The capillary and sample can be aligned and scanned with nanometer precision using a piezo-based manipulator with 11 degrees of freedom [SmarAct]. A rendering of the microARPES measurement geometry is presented in **Figure 1b**.

As a starting point, the electronic structures of bulk MnBi_2Te_4 and $\text{Mn}(\text{Sb}_d\text{Bi}_{1-d})_2\text{Te}_4$ with a nominal mole fraction given by $d = 0.3$ are considered to establish the doping-dependent low-energy spectra of MBTs in our measurement configuration. **Figure 1c** presents an optical micrograph image of the $\text{Mn}(\text{Sb}_d\text{Bi}_{1-d})_2\text{Te}_4$ crystal glued to the sample holder. The same crystal has been cleaved in the microARPES ultra-high vacuum end-station and scanned under the microscopic beam using a photon energy of 100 eV, which enables mapping of the spatially-dependent photoemission intensity of the Te $4d$ and Sb $4d$ core level and low-energy BVB and BCB regions. The (x, y) -dependent intensity in **Figure 1d** is a projection of the (E, k) -region on the detector containing the Te $4d$ core level, which produces a map of the entire crystal in correspondence with the optical image. Each point on the map contains a core level spectrum as shown for two representative areas in **Figure 1e**. The variation of intensity in the map is caused by a combination of insufficiently cleaved areas and core level shifts that move the peak intensity out of the (E, k) -integration region of the map. Shifts of up to 100 meV are observed as shown via the red and blue curves in **Figure 1e**. The corresponding low-energy spectra and Fermi surfaces are presented in **Figure S1**, which exhibit consistent doping effects. These observations highlight the local inhomogeneity of Sb substitution and resulting doping at the probed surface, which necessitates the use of microARPES to resolve the electronic structure.

The low-energy dispersion and Fermi surface from the area marked by a red circle in **Figure 1d** are compared with those of a bulk MnBi_2Te_4 crystal in **Figures 1f–g**. The sharp “v”-shaped bands of MnBi_2Te_4 correspond to the BVB and BCB, which display an energy gap with a peak-to-peak separation of 150 meV. The topological state is not visible in the gap at the photon energy of 21 eV used here due to strong matrix element effects.^[24] A pair of faint parabolic bands are visible near the Fermi level,

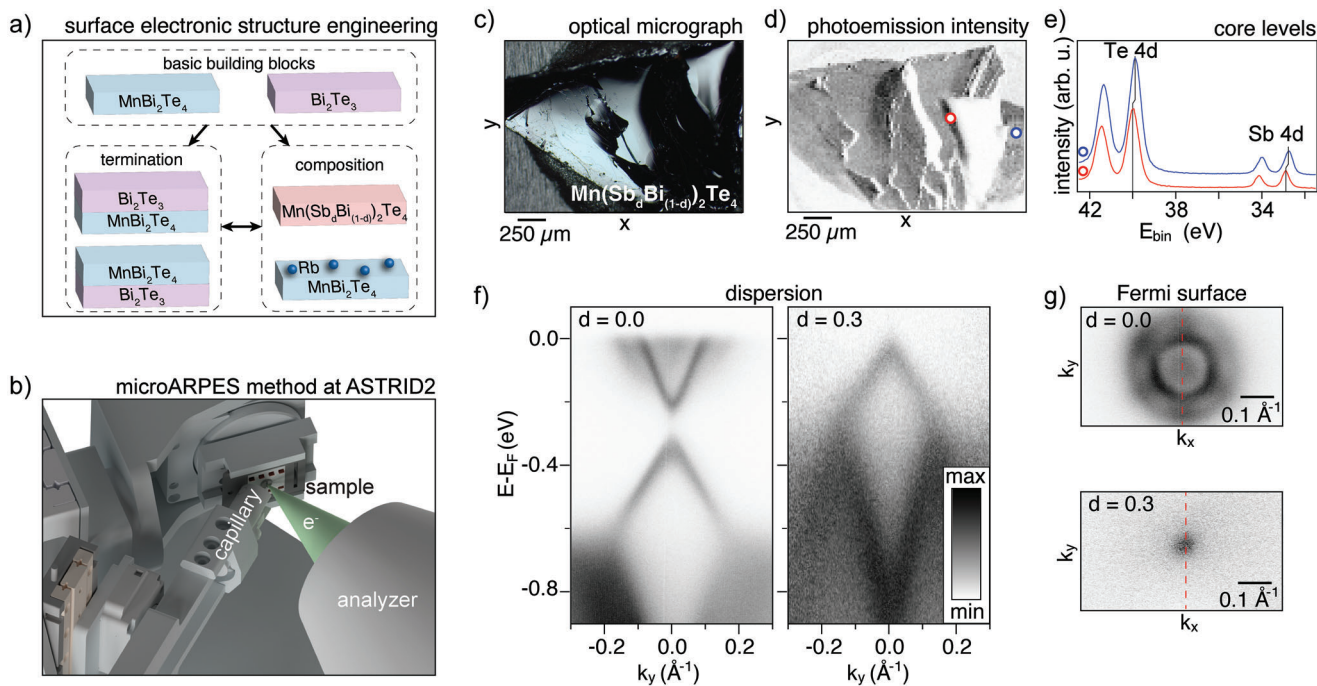


Figure 1. Characterization of manganese bismuth tellurides by microARPES. a) Overview of methods to tailor the surface electronic structure of MBTs based on MnBi_2Te_4 and Bi_2Te_3 building blocks. b) Rendering of the microARPES measurement configuration at the new SGM4 beamline of the ASTRID2 light source. The green cone illustrates photoemitted electrons (e^-) from a microscopic spot on the sample. c) Optical image of $\text{Mn}(\text{Sb}_d\text{Bi}_{1-d})_2\text{Te}_4$ with a nominal Sb mole fraction of $d = 0.3$. d) Map of (x, y) -dependent photoemission intensity of the Te 4d core level obtained at a photon energy of 100 eV corresponding to the area imaged in (c). e) Core level spectra extracted from the positions marked by blue and red circles in (d). The vertical bars mark a shift of 100 meV between the two spectra. f)–g) ARPES dispersions and Fermi surfaces obtained from crystals with $d = 0.0$ and $d = 0.3$, highlighting the significant impact of Sb substitution on doping. The (E, k_y) -dependent cuts in (f) were extracted along the dashed red lines in (g). The photon energy for the spectra in (f)–(g) is 21 eV for $d = 0.0$ and 16.2 eV for $d = 0.3$.

E_F , which have previously been described on the basis of laser-based ARPES as a pair of Rashba-type surface bands that are strongly hybridized with the topological state.^[28] A six-fold set of lobes appear in the Fermi surface from these states, in addition to near-circular features from BCB states. The Sb substituted crystal simply displays the “v”-shaped BVB around E_F and a point-like Fermi surface, providing an ideal situation for electron transport or optical pump-probe experiments involving the topological state. However, given the spatial doping inhomogeneity, additional means to fine control the doping would be required in a hypothetical transport experiment involving such a sample. In the following, we consider Rb deposition on pristine MBTs as an alternative method to tune the low-energy band structure.

The effect of in situ Rb deposition on MnBi_2Te_4 is tracked via energy distribution curves (EDCs) extracted at normal emission and plotted against Rb coverage, as shown in **Figure 2a**. Calibration of a complete Rb monolayer (ML) is determined to be the point at which the Rb 3d core level peak position stops increasing linearly and the linewidth remains constant, as presented in Figure S2 (Supporting Information). Note that 0 ML indicates the instant where the shutter is opened and the surface is exposed to Rb atoms. Data shown before 0 ML represent a baseline for the situation without adsorbed Rb atoms. Representative snapshots of the (E, k) -dependent dispersion at different Rb coverages are shown in Figure 2b. Initially, the BVB and BCB edges shift rigidly down by a maximum of around 25 meV at 0.2 ML, signifying mi-

nuscle electron-doping by the adsorbed Rb atoms. Upon further increase of the Rb coverage, the bands surprisingly shift back toward E_F . At 0.5 ML, the BVB and BCB edges are back to their original position. Beyond 0.8 ML, two features start to emerge in the bulk gap. They are most clearly seen at a coverage of 1.25 ML in Figure 2b, where they are marked by blue arrows. A possible explanation of these features is that they reflect emerging photoemission intensity from the robust topological bands as the adsorbed Rb atoms destroy the remaining surface states and their hybridization with the topological bands. The changed surface potential due to the Rb adatoms also influences the photoemission matrix elements, potentially causing the emergence of intensity from the topological states at our photon energy of 21 eV. Intriguingly, a peak-to-peak separation of 45 meV is determined between the features, which could hint at a doping-dependent gapped crossing between the topological bands.^[35] An alternative explanation involves Rb-induced surface band bending and the appearance of quantum well states of the BVB and BCB.^[44] However, this appears rather unlikely given the reduced amount of doping. The entire Rb deposition sequence can be viewed as divided into two stages, as marked by green and purple arrows in Figure 2a: An initial electron-doping stage with rigid energy shifts in the dilute limit, followed by hole-doping and dramatic electronic structure changes in the dense limit. The hole-doping stage is unexpected as one would normally anticipate alkali metals to merely donate electrons at the surface.

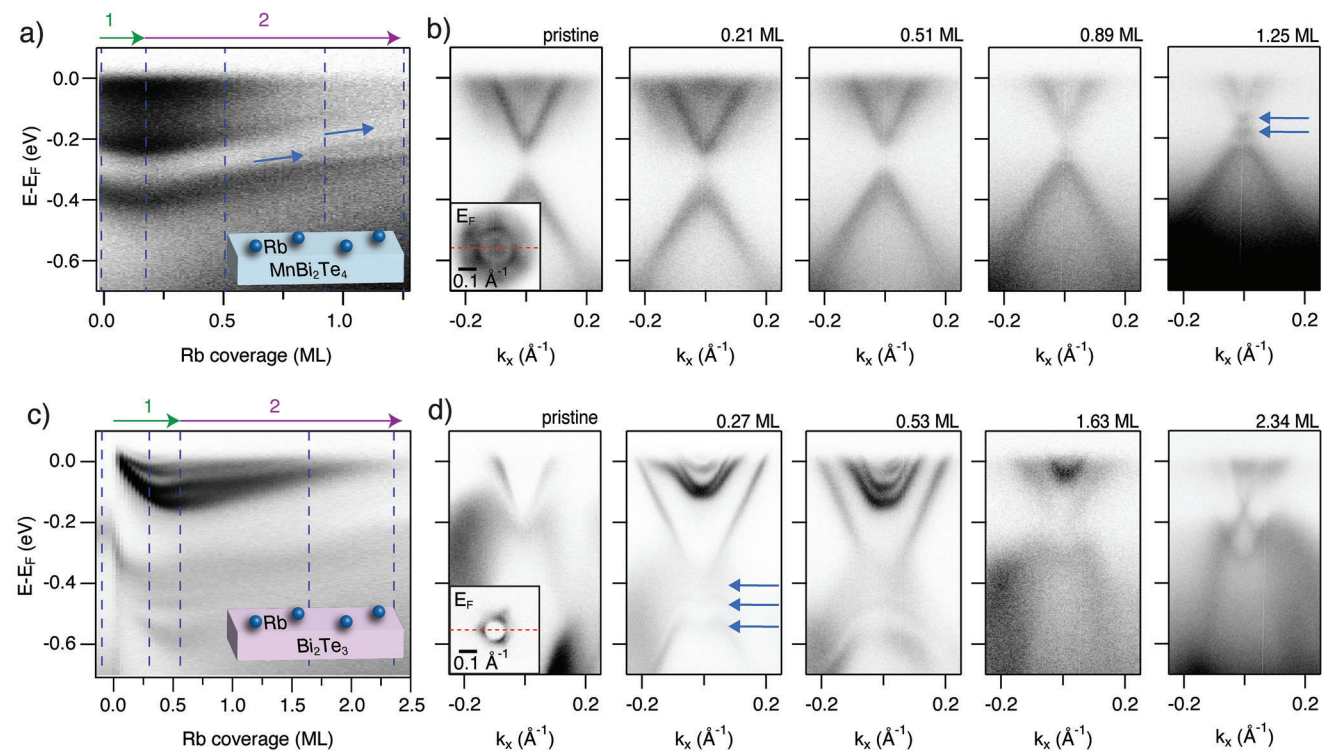


Figure 2. Surface electronic structure modification of bulk MnBi_2Te_4 and Bi_2Te_3 during in situ Rb deposition. a) EDCs of the ARPES intensity of MnBi_2Te_4 at normal emission as a function of Rb coverage. b) ARPES spectra of MnBi_2Te_4 at the given Rb coverages, demarcated by vertical dashed lines in (a). Blue arrows in (a)-(b) demarcate features in the bulk gap. c,d) ARPES measurements of Bi_2Te_3 during Rb deposition presented in the same way as for MnBi_2Te_4 in (a)-(b). Blue arrows demarcate replicas of the valence band induced by surface band bending. Green and purple arrows in (a) and (c) indicate electron and hole stages of doping, respectively. The spectra in (b) and (d) were extracted along the dashed red lines shown in the Fermi surface insets in the panels with the pristine dispersion. The data are obtained at a photon energy of 21 eV.

The experiment is repeated on the quintuple layer building block of the MBTs, i.e. Bi_2Te_3 , in order to gain further insights on the Rb coverage-dependent effects and their impact on the low-energy dispersion of these materials. Two stages of doping following a similar sequence as for MnBi_2Te_4 are observed but with more striking changes to the low-energy dispersion as shown in Figure 2c,d. Pristine Bi_2Te_3 exhibits linear bands dispersing to E_F , which correspond to the topological surface state. The bands cross just below the edge of the broad “M”-shaped continuum of states that reflect the BVB.^[45,46] Deposition of Rb initially leads to strong electron-doping with bands shifting 230 meV to higher binding energies concomitant with the appearance of several sharp parabolic states near E_F . Additionally, several “M”-shaped replicas of the BVB appear, as marked by blue arrows on the 0.27 ML spectrum in Figure 2d. These features are interpreted as quantum well states induced by strong surface band bending, as described in similar experiments on Bi_2Se_3 .^[47] As the Rb coverage is increased beyond 0.5 ML, the bands shift back toward E_F , the BCB occupation strongly decreases and the quantum well states disappear. At an extreme Rb coverage of 2.34 ML, the topological surface state is observed with a modified dispersion compared to the pristine case, and the topological bands exhibit a crossing above the BVB edge. The behaviors observed at extreme Rb coverages on both MnBi_2Te_4 and Bi_2Te_3 are indicative of a complex interaction between the adsorbed Rb and the surface lay-

ers of the materials, possibly hinting at Rb intercalation in the van der Waals gap or alloying between the materials.

The surface character of the Rb-induced states in MnBi_2Te_4 can be further verified by a flat dispersion with photon energy. In order to establish a comparison, we first present the photon energy dependent dispersion of pristine MnBi_2Te_4 at normal emission in Figure 3a. The dominant features are the dispersing BCB and BVB edges, which have been highlighted by dashed red curves. Figure 3b presents ARPES spectra at three pertinent photon energies, providing ideal matrix elements for visualizing the topological surface state ($h\nu = 15.0$ eV), and revealing the maximum ($h\nu = 17.3$ eV) and minimum ($h\nu = 20.6$ eV) of the bulk bandgap. These key features are marked by green and red arrows, respectively. Our observations are fully in line with previous synchrotron studies of MnBi_2Te_4 .^[4] At an Rb coverage of 1.85 ML, deep in the second stage of doping, we primarily observe non-dispersing states with photon energy, as shown in Figure 3c,d and highlighted by blue arrows. Note that the near-vertical features in the intensity around photon energies of 19 and 24 eV in Figure 3c stem from core level photoemission. The lack of dispersion is a strong indication for the surface-derived nature of the states at high Rb coverages.

To further elucidate the interaction between Rb and the surface of MnBi_2Te_4 , measurements of core level spectra as a function of Rb coverage are performed. Surveys obtained with a

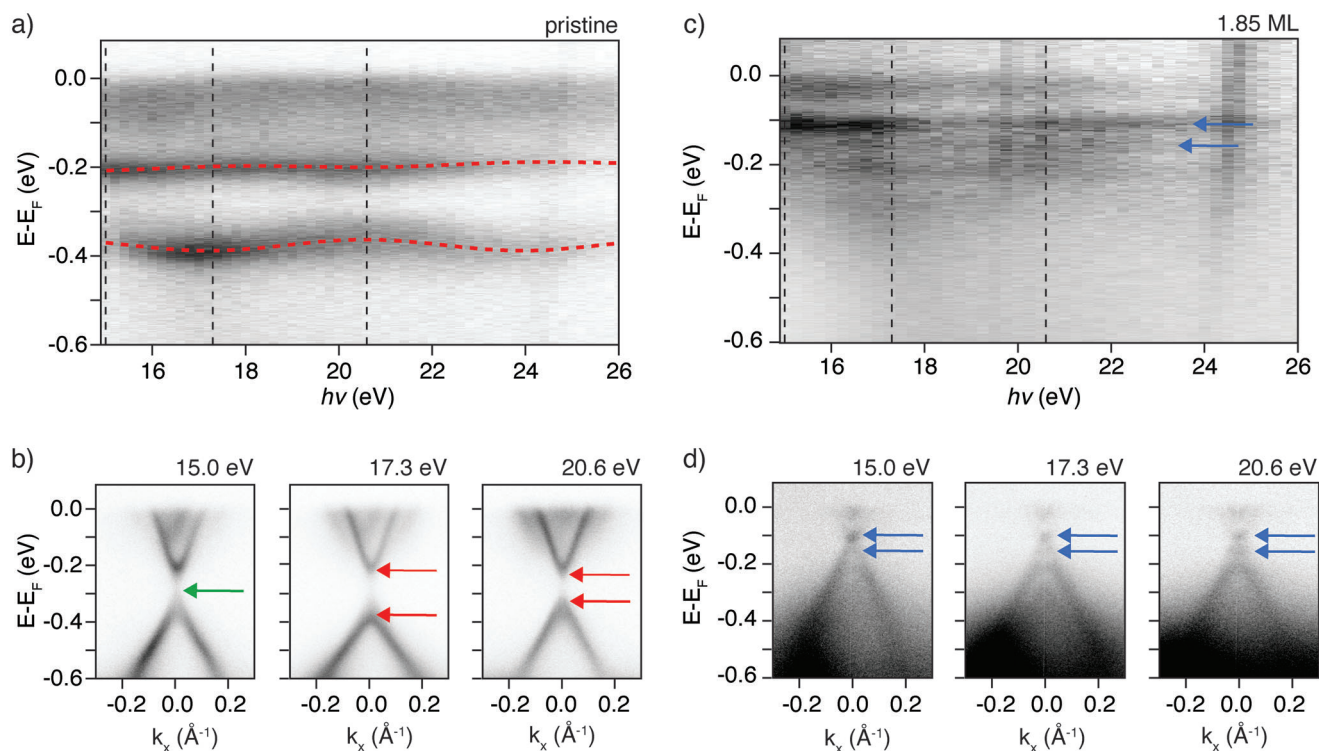


Figure 3. Photon energy dependence of MnBi_2Te_4 ARPES dispersion. a) EDCs of the ARPES intensity of pristine MnBi_2Te_4 at normal emission as a function of photon energy. Dashed red curves demarcate the BCB and BVB edges. b) ARPES spectra taken at the given photon energies. The green arrow indicates the appearance of the topological surface state. The red arrows outline the shift of the BCB and BVB edges with photon energy. c,d) Corresponding spectra of MnBi_2Te_4 with an Rb coverage of 1.85 ML. The blue arrows indicate the emergent in-gap surface states. The color scale in (c) has been normalized to enhance the contrast of the low-energy features.

photon energy of 145 eV before and after deposition are shown in **Figure 4a**, providing an overview of accessible core levels in the experiment. During Rb deposition, the intensity of the Bi 5*d* and Te 4*d* peaks decreases linearly while the Rb 3*d* peak intensity grows steadily with a single doublet shifting in binding energy, as seen in **Figure 4b**. These monotonic behaviors of the intensity in combination with the absence of an additional set of Rb 3*d* components rule out intercalation of Rb in the van der Waals gap of the crystal.^[47] In the dense limit, a side-peak appears on the Bi 5*d* core level, as demarcated by grey arrows in **Figure 4b**. Extracted Bi 5*d* and Te 4*d* core level shifts are presented together with the BVB shift as a function of Rb coverage in **Figure 4c**. All shifts follow similar trends and are of comparable magnitudes, indicating that the binding energy positions of the peaks are mainly determined by doping.^[48] The Bi 5*d* side-peaks appear to split out from the main set of peaks with an increasing energy separation between main and side-peaks in the dense limit. This behavior is indicative of alloy formation,^[7] similarly as observed when dosing Ti on Bi_2Se_3 ,^[49] which results in hole doping and dramatic changes of the surface electronic structure. The hole-doping effect could also be explained by the formation of a surface metallic film by the adsorbed Rb that leads to a depolarization of the surface dipole.^[50] In this case, one would expect an increase in the asymmetry of the Te 4*d* core level lineshape, however, this is found to decrease with coverage as shown in **Figure S2** (Supporting Information), which speaks for the formation of an alloy. These results emphasize that alkali doping is a complex process in general. Even in

the early stages of doping, it is possible that a chemical bond is formed between the alkali and the surface layer of the material, which has previously been shown to lead to unexpected band gap sizes in alkali-doped semiconductors.^[40,41,51]

Having assessed the impact of Rb adsorption on the separate MnBi_2Te_4 and Bi_2Te_3 systems, the surface electronic structure changes of the corresponding terminations on the MnBi_4Te_7 heterostructure are now examined. The two terminations are distinguished by their unique surface electronic states. To optimally bring out the details of their complex band structures, we have surveyed the low-energy spectra as a function of photon energy, as shown in **Figure S3** (Supporting Information). Starting with the Rb dosing sequence on the Bi_2Te_3 termination, the evolution of the surface electronic structure is tracked via EDCs in **Figure 5a**. Two stages of doping are again identified with an initial downwards shift of the bands due to electron-doping, followed by hole-doping and a significant reduction of photoemission intensity. It is noted that the evolution of the intensity during the second stage exhibits similar behavior on the MnBi_2Te_4 termination, which is discussed in further detail below and in **Figure S4** (Supporting Information). Concentrating on the electron-doping stage, a series of ARPES spectra from pristine to maximum electron-doping at 0.44 ML are presented together with second-derivative plots of the intensity in **Figure 5b–d**. Bands of different character are highlighted by colored dashed curves on the second-derivative data. In the pristine state, the central features are a surface band hybridization gap (red dashed curves), a pair

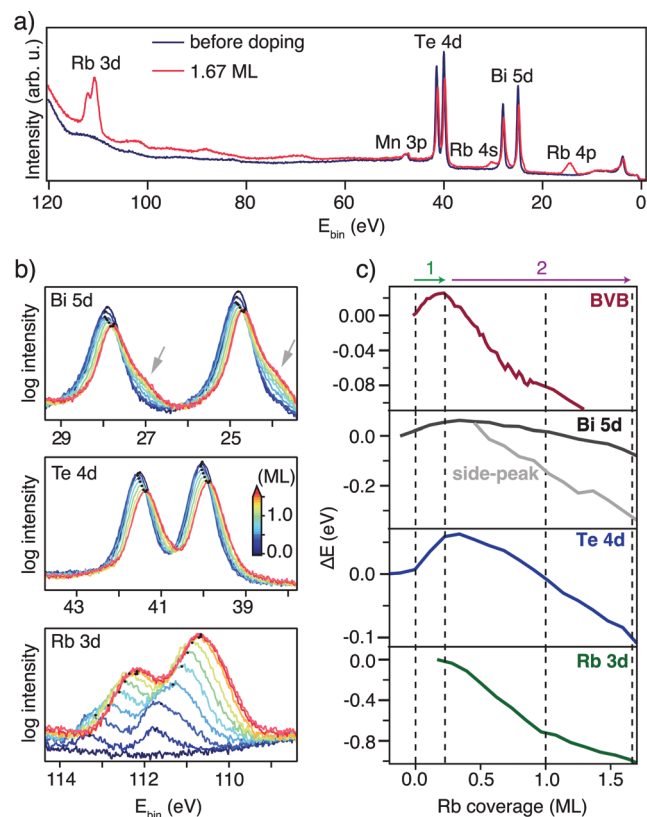


Figure 4. Core level analysis of the interaction between Rb and MnBi_2Te_4 . a) Survey of MnBi_2Te_4 core levels measured at a photon energy of 145 eV before Rb dosing and at a coverage of 1.67 ML. b) Bi 5d, Te 4d and Rb 3d core level spectra as a function of Rb coverage, as given by the color scale. The grey arrows demarcate side-peaks emerging on the Bi 5d core levels. The intensity is plotted on a logarithmic scale. The black dots mark fitted core level peak positions. c) Core level shifts extracted from the spectra in (b) as well as the shift of BVB position obtained from Figure 2a plotted against Rb coverage.

of surface bands that cross E_F (blue dashed curves) as well as BVB and BCB states (orange dashed curves).^[2,18,23,26,27] Upon Rb deposition, the surface states around E_F and the hybridized surface bands shift by up to 150 meV toward higher binding energies while the bulk bands merely exhibit shifts of 50 meV, as seen in Figure 5c,d. This causes the surface hybridization gap to close, giving rise to a region of increased intensity around -0.38 eV. The doping-dependent behavior and modification of surface electronic structure seen here are highly similar to a previous observation of photoinduced filling of the surface hybridization gap on the Bi_2Te_3 termination of MnBi_4Te_7 ,^[13] suggesting that this gap is extremely fragile toward external stimuli that alter the carrier concentration.

Turning toward the MnBi_2Te_4 termination of MnBi_4Te_7 , the coverage-dependent EDCs at normal emission are shown in Figure 6a, which again reveals the trend of electron-doping followed by hole-doping. ARPES spectra are presented in Figure 6b for the clean surface, the maximally electron-doped surface at 0.34 ML as well as two spectra in the second stage with coverages of 0.74 ML and 1.74 ML. Fermi surfaces are displayed in Figure 6c for the pristine sample and in the case of a coverage

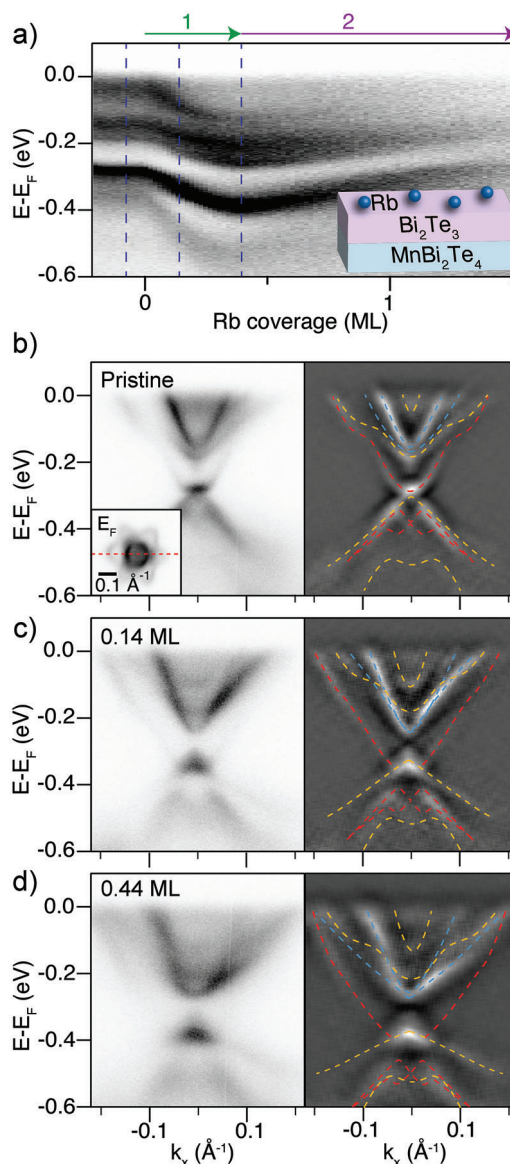


Figure 5. Rb deposition and electron-doping tracked on the Bi_2Te_3 termination of MnBi_4Te_7 . a) EDCs at normal emission as a function of Rb coverage. b–d) ARPES spectra (left panels) and corresponding second-derivative of the intensity (right panels) for the stated Rb coverages. The colored overlays are a guide to the eye inferred from the second-derivative features, highlighting hybridized surface bands (red dashed curves), trivial surface states (blue dashed curves) as well as the BVB and BCB (orange dashed curves). The dashed lines in (a) mark the coverages in (b)–(d). The spectra were extracted along the dashed red line shown in the inset with the Fermi surface in (b). The photon energy applied for the measurements is 18 eV.

of 1.74 ML. In the pristine case, the main distinguishing feature of the MnBi_2Te_4 termination is a surface-induced Rashba-like state, which forms the outer circle in the Fermi surface.^[18] The feature is marked by pink arrows in Figure 6b–c. Similarly as in bulk MnBi_2Te_4 , the topological surface state is situated in the bulk gap around 300 meV below E_F with its photoemission intensity strongly suppressed above photon energies of 16 eV.^[18] The

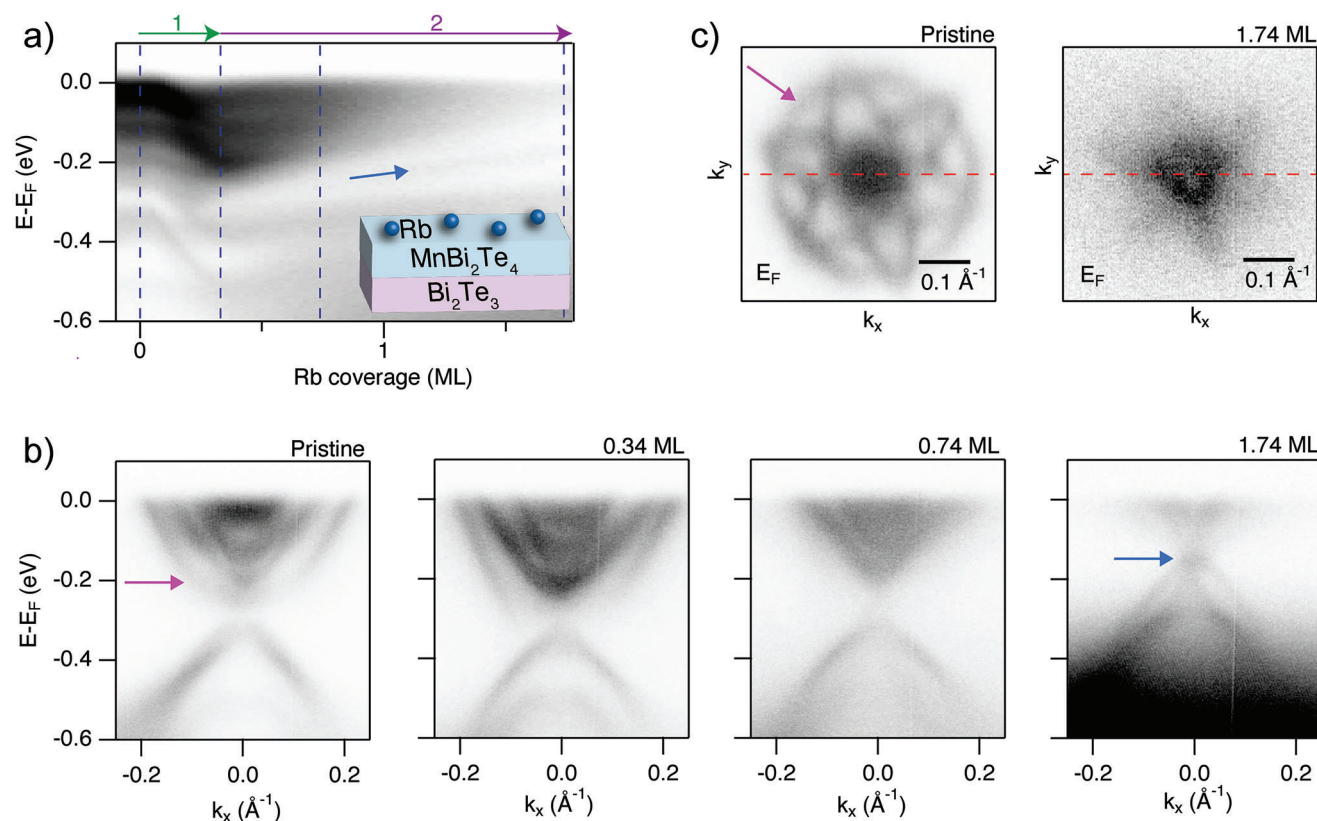


Figure 6. Tuning the surface electronic structure on the $MnBi_2Te_4$ termination of $MnBi_4Te_7$. a) EDCs at normal emission as a function of Rb coverage. b) ARPES spectra at the given Rb coverages (see dashed vertical lines in (a)). c) Fermi surface before deposition and at a Rb coverage of 1.74 ML. The dashed red lines demarcate the cut direction for the spectra shown in (b). Blue arrows in (a) and (b) indicate emerging intensity in the bulk band gap. Pink arrows in (b) and (c) point to a Rashba-like state that is characteristic of the $MnBi_2Te_4$ termination. The spectra were collected using a photon energy of 21 eV.

main effect of the adsorbed Rb on this termination appears to be a removal of the surface bands, including the Rashba-like state, which have completely vanished at a coverage of 0.74 ML. Intriguingly, intensity emerges in the region of the bulk gap when the coverage is further increased. This is exemplified by the spectrum at 1.74 ML, which reveals the intensity to stem from a pair of crossing bands, as seen via the blue arrow in Figure 6b. Spectra at high coverages exhibit emerging photoemission intensity from topological bands on both terminations of $MnBi_4Te_7$, as shown in Figure S4 (Supporting Information), which is consistent with the surface-specific bands having been destroyed by the reaction between Rb and the surface layers. This suggests that the remaining features are the BVB and BCB in addition to a set of crossing topological bands.

Interestingly, the appearance of persistent topological bands within 200 meV of E_F seems to be a common feature between bulk $MnBi_2Te_4$, Bi_2Te_3 and their terminations on $MnBi_4Te_7$ at extreme Rb coverages. A peculiarity of $MnBi_2Te_4$ is the relatively insignificant changes occurring during stage 1 of doping compared to the other systems. Additionally, maximum electron-doping of $MnBi_2Te_4$ occurs around an Rb coverage of 0.2 ML, which is lower than observed in the other materials. A key reason for these differences is that we mainly observe the bulk states of $MnBi_2Te_4$ during stage 1 of doping and these are less sensitive

to the adsorbed Rb than the surface-derived bands that dominate the ARPES spectra of Bi_2Te_3 and $MnBi_4Te_7$. Furthermore, it is possible that the adsorbate structures of Rb can vary between the surfaces, giving rise to different doping behaviors with coverage. The dramatic modifications of surface electronic structures with alkali adsorption during stage 2 of doping likely impact the magnetic properties of $MnBi_2Te_4$ and $MnBi_4Te_7$, which will be interesting to probe across the Néel temperature with high-resolution laser-based microARPES operating in the sub-10 K temperature regime, as recently demonstrated on the pristine systems.^[12]

3. Conclusion

In conclusion, the surface electronic structures of the MBT building blocks $MnBi_2Te_4$ and Bi_2Te_3 and their terminations on $MnBi_4Te_7$ were resolved in situ using microARPES at the new SGM4 beamline at the ASTRID2 light source during deposition of the alkali metal Rb. In all situations, two stages of doping are observed with an initial electron-doping effect, which is then followed by a hole-doping effect. Core level measurements indicate that significant alloying between Rb and the surface layers occurs at high coverages, which further drives dramatic band structure changes, including the removal of surface states and hybridization effects. On the Bi_2Te_3 termination of $MnBi_4Te_7$, a closing of

the surface hybridization gap is induced before the surface electronic structure organizes into a minimal configuration with just the BVB and BCB remaining in addition to the robust topological bands. Further studies of the effects of alkali deposition on MBTs may additionally reveal the nature of the surviving topological bands and what role the alloy plays. The examples presented here underline the extreme tunability and sensitivity of the surface electronic states of the MBTs toward external stimuli, which could potentially be exploited for further developing the quantum transport phenomena in functioning MBT devices.

4. Experimental Section

Crystal Growth: Single crystals were grown using the Bi_2Te_3 flux method, as previously reported in Ref. [14] for MnBi_2Te_4 and MnBi_4Te_7 and Ref. [45] for Bi_2Te_3 . To synthesize crystals of $\text{Mn}(\text{Sb}_d\text{Bi}_{1-d})_2\text{Te}_4$, the elemental starting materials of Mn, Sb, Bi, and Te were mixed and sealed in a vacuum quartz tube. The tube was subsequently heated to 900 °C, slowly cooled to 601 °C, and then canted to remove the flux.

Photoemission Measurements: The microARPES measurements were performed at the SGM4 beamline of the ASTRID2 synchrotron radiation source at Aarhus University, Denmark.^[43] The MnBi_2Te_4 , MnBi_4Te_7 , and Bi_2Te_3 crystals were cleaved in situ and measured at a temperature of 120 K in a base pressure better than $1 \cdot 10^{-10}$ mbar. The $\text{Mn}(\text{Sb}_d\text{Bi}_{1-d})_2\text{Te}_4$ samples were cleaved in situ at room temperature and a base pressure better than $5 \cdot 10^{-8}$ mbar. ARPES and core level spectra were collected using a SPECS Phoibos 150 SAL analyzer. Measurements of the (E, k_x, k_y) -dependent photoemission intensity were performed using the scanning angle lens feature of the analyzer while the sample position was held fixed. The applied photon energies were in the range of 16–21 eV for the ARPES spectra, while the core level measurements were performed with 145 eV, except in Figure 1e where 100 eV was applied. The light polarization was predominantly linear horizontal. The energy- and angular resolution were better than 20 meV and 0.1°, respectively. The second-derivative ARPES intensity was produced using the method described in Ref. [52]. Rb adatoms were deposited from a SAES alkali getter during measurements. The Rb coverage was estimated by comparing the Te 4d and Rb 3d core level areas before and after a deposition cycle. The point at which the peak position of the Rb 3d core level stopped shifting linearly and the linewidth remained constant is taken as an indication for an ordered structure corresponding to 1 ML, as shown in Figure S2 (Supporting Information). The ratio of the area growth rates for the Te 4d and Rb 3d core levels at this coverage was then used as calibration for calculating the Rb coverage from the change of the Te 4d area at each dosing step.

Statistical Analysis: The raw ARPES spectra were transformed from angle to momentum coordinates, and a Fermi level correction was applied based on reference spectra of polycrystalline tantalum. Core level spectra were fitted with a Doniach-Šunjić function with a linear background at every point of the Rb deposition series. The data was plotted and analyzed using WaveMetrics IGOR Pro 7 software.

Supporting Information

Supporting Information is available from the Wiley Online Library or from the author.

Acknowledgements

K.V. and P.M. contributed equally to this work. The authors are grateful for the support from the mechanical workshop at the Department of Physics and Astronomy, Aarhus University, during the design and construction of the microARPES beamline, as well as discussions on technical implementation with Aaron Bostwick, Chris Jozwiak, Eli Rotenberg, Pavel Dudin,

Matthew Watson, and Cephise Cacho. The authors thank MaxLab and in particular Balasubramanian Thiagarajan, Johan Adell and Jesper Andersen for the MaxLab 14 beamline, as well as David Field for the SGM2 chambers, which were now all of the new SGM4 beamline. Xing-Chen Pan would like to thank Bo Chen, Fucong Fei, and Fengqi Song for their helpful discussion. The authors acknowledge funding from VILLUM FONDEN through the Young Investigator Program (Grant. no. 15375), Villum Investigator Program (Grant. no. 25931) and the Centre of Excellence for Dirac Materials (Grant. no. 11744), and the Danish Council for Independent Research, Natural Sciences under the Sapere Aude program (Grant nos. DFF-6108-00409 and DFF-9064-00057B), and from the Aarhus University Research Foundation. Work at Advanced Institute for Materials Research had benefited from support of WPI-AIMR, JSPS KAKENHI Basic Science A (22H00278, 21K18590, 20H04623, 18H04473, 18H03858, and 18F18328) and Tohoku University FRID program.

Conflict of Interest

The authors declare no conflict of interest.

Data Availability Statement

The data that support the findings of this study are available from the corresponding author upon reasonable request.

Keywords

alkali doping, magnetic topological insulators, microARPES, surface band structure engineering, tunable topological bands

Received: February 28, 2023

Revised: April 8, 2023

Published online:

- [1] M. M. Otrokov, I. I. Klimovskikh, H. Bentmann, D. Estyunin, A. Zeugner, Z. S. Aliev, S. Gaß, A. U. B. Wolter, A. V. Koroleva, A. M. Shikin, M. Blanco-Rey, M. Hoffmann, I. P. Rusinov, A. Y. Vyazovskaya, S. V. Ereemeev, Y. M. Koroteev, V. M. Kuznetsov, F. Freyre, J. Sánchez-Barriga, I. R. Amiraslanov, M. B. Babanly, N. T. Mamedov, N. A. Abdullayev, V. N. Zverev, A. Alfonsov, V. Kataev, B. Büchner, E. F. Schwier, S. Kumar, A. Kimura, et al., *Nature* **2019**, 576, 416.
- [2] I. I. Klimovskikh, M. M. Otrokov, D. Estyunin, S. V. Ereemeev, S. O. Filnov, A. Koroleva, E. Shevchenko, V. Voroshnin, A. G. Rybkin, I. P. Rusinov, M. Blanco-Rey, M. Hoffmann, Z. S. Aliev, M. B. Babanly, I. R. Amiraslanov, N. A. Abdullayev, V. N. Zverev, A. Kimura, O. E. Tereshchenko, K. A. Kokh, L. Petaccia, G. Di Santo, A. Ernst, P. M. Echenique, N. T. Mamedov, A. M. Shikin, E. V. Chulkov, *npj Quantum Mater.* **2020**, 5, 54.
- [3] Y. An, K. Wang, S. Gong, Y. Hou, C. Ma, M. Zhu, C. Zhao, T. Wang, S. Ma, H. Wang, R. Wu, W. Liu, *npj Comput. Mater.* **2021**, 7, 45.
- [4] B. Chen, F. Fei, D. Zhang, B. Zhang, W. Liu, S. Zhang, P. Wang, B. Wei, Y. Zhang, Z. Zuo, J. Guo, Q. Liu, Z. Wang, X. Wu, J. Zong, X. Xie, W. Chen, Z. Sun, S. Wang, Y. Zhang, M. Zhang, X. Wang, F. Song, H. Zhang, D. Shen, B. Wang, *Nat. Commun.* **2019**, 10, 4469.
- [5] Y. Deng, Y. Yu, M. Z. Shi, Z. Guo, Z. Xu, J. Wang, X. H. Chen, Y. Zhang, *Science* **2020**, 367, 895.
- [6] X.-M. Ma, Y. Zhao, K. Zhang, S. Kumar, R. Lu, J. Li, Q. Yao, J. Shao, F. Hou, X. Wu, M. Zeng, Y.-J. Hao, Z. Hao, Y. Wang, X.-R. Liu, H. Shen, H. Sun, J. Mei, K. Miyamoto, T. Okuda, M. Arita, E. F. Schwier, K. Shimada, K. Deng, C. Liu, J. Lin, Y. Zhao, C. Chen, Q. Liu, C. Liu, *Phys. Rev. B* **2021**, 103, L121112.

- [7] A. Liang, C. Chen, H. Zheng, W. Xia, K. Huang, L. Wei, H. Yang, Y. Chen, X. Zhang, X. Xu, M. Wang, Y. Guo, L. Yang, Z. Liu, Y. Chen, *Nano Lett.* **2022**, *22*, 4307.
- [8] J. Wu, F. Liu, M. Sasase, K. Ienaga, Y. Obata, R. Yukawa, K. Horiba, H. Kumigashira, S. Okuma, T. Inoshita, H. Hosono, *Sci. Adv.* **2019**, *5*, eaax9989.
- [9] C. X. Trang, Q. Li, Y. Yin, J. Hwang, G. Akhgar, I. Di Bernardo, A. Grubišić-Čabo, A. Tadich, M. S. Fuhrer, S.-K. Mo, N. V. Medhekar, M. T. Edmonds, *ACS Nano* **2021**, *15*, 13444.
- [10] R. Xu, Y. Bai, J. Zhou, J. Li, X. Gu, N. Qin, Z. Yin, X. Du, Q. Zhang, W. Zhao, Y. Li, Y. Wu, C. Ding, L. Wang, A. Liang, Z. Liu, Y. Xu, X. Feng, K. He, Y. Chen, L. Yang, *Nano Lett.* **2022**, *22*, 6320.
- [11] D. Nevola, H. X. Li, J.-Q. Yan, R. G. Moore, H.-N. Lee, H. Miao, P. D. Johnson, *Phys. Rev. Lett.* **2020**, *125*, 117205.
- [12] C. Yan, E. Green, R. Fukumori, N. Protic, S. H. Lee, S. Fernandez-Mulligan, R. Raja, R. Erdakos, Z. Mao, S. Yang, *Rev. Sci. Instrum.* **2021**, *92*, 113907.
- [13] H. Zhong, C. Bao, H. Wang, J. Li, Z. Yin, Y. Xu, W. Duan, T.-L. Xia, S. Zhou, *Nano Lett.* **2021**, *21*, 6080.
- [14] P. E. Majchrzak, Y. Liu, K. Volckaert, D. Biswas, C. Sahoo, D. Puntel, W. Bronsch, M. Tuniz, F. Cilento, X.-C. Pan, Q. Liu, Y. P. Chen, S. Ulstrup, *Nano Lett.* **2023**, *23*, 414.
- [15] L. Jiaheng, L. Yang, D. Shiqiao, W. Zun, G. Bing-Lin, Z. Shou-Cheng, H. Ke, D. Wenhui, X. Yong, *Sci. Adv.* **2019**, *5*, eaaw5685.
- [16] J. Wu, F. Liu, C. Liu, Y. Wang, C. Li, Y. Lu, S. Matsuishi, H. Hosono, *Adv. Mater.* **2020**, *32*, 2001815.
- [17] C. Hu, K. N. Gordon, P. Liu, J. Liu, X. Zhou, P. Hao, D. Narayan, E. Emmanouilidou, H. Sun, Y. Liu, H. Brawer, A. P. Ramirez, L. Ding, H. Cao, Q. Liu, D. Dessau, N. Ni, *Nat. Commun.* **2020**, *11*, 1.
- [18] X. Wu, J. Li, X.-M. Ma, Y. Zhang, Y. Liu, C.-S. Zhou, J. Shao, Q. Wang, Y.-J. Hao, Y. Feng, E. F. Schwier, S. Kumar, H. Sun, P. Liu, K. Shimada, K. Miyamoto, T. Okuda, K. Wang, M. Xie, C. Chen, Q. Liu, C. Liu, Y. Zhao, *Phys. Rev. X* **2020**, *10*, 031013.
- [19] R. C. Vidal, A. Zeugner, J. I. Facio, R. Ray, M. H. Haghighi, A. U. B. Wolter, L. T. Corredor Bohorquez, F. Cagliaris, S. Moser, T. Figgemeier, T. R. F. Peixoto, H. B. Vasili, M. Valvidares, S. Jung, C. Cacho, A. Alfonsov, K. Mehlatat, V. Kataev, C. Hess, M. Richter, B. Büchner, J. van den Brink, M. Ruck, F. Reinert, H. Bentmann, A. Isaeva, *Phys. Rev. X* **2019**, *9*, 041065.
- [20] H. Sun, B. Xia, Z. Chen, Y. Zhang, P. Liu, Q. Yao, H. Tang, Y. Zhao, H. Xu, Q. Liu, *Phys. Rev. Lett.* **2019**, *123*, 096401.
- [21] H. Deng, Z. Chen, A. Wołos, M. Konczykowski, K. Sobczak, J. Sitnicka, I. V. Fedorchenko, J. Borysiuk, T. Heider, Ł. Pluciński, K. Park, A. B. Georgescu, J. Cano, L. Krusin-Elbaum, *Nat. Phys.* **2021**, *17*, 36.
- [22] C. Liu, Y. Wang, H. Li, Y. Wu, Y. Li, J. Li, K. He, Y. Xu, J. Zhang, Y. Wang, *Nat. Mater.* **2020**, *19*, 522.
- [23] H. Li, S.-Y. Gao, S.-F. Duan, Y.-F. Xu, K.-J. Zhu, S.-J. Tian, J.-C. Gao, W.-H. Fan, Z.-C. Rao, J.-R. Huang, J.-J. Li, D.-Y. Yan, Z.-T. Liu, W.-L. Liu, Y.-B. Huang, Y.-L. Li, Y. Liu, G.-B. Zhang, P. Zhang, T. Kondo, S. Shin, H.-C. Lei, Y.-G. Shi, W.-T. Zhang, H.-M. Weng, T. Qian, H. Ding, *Phys. Rev. X* **2019**, *9*, 041039.
- [24] Y. J. Chen, L. X. Xu, J. H. Li, Y. W. Li, H. Y. Wang, C. F. Zhang, H. Li, Y. Wu, A. J. Liang, C. Chen, S. W. Jung, C. Cacho, Y. H. Mao, S. Liu, M. X. Wang, Y. F. Guo, Y. Xu, Z. K. Liu, L. X. Yang, Y. L. Chen, *Phys. Rev. X* **2019**, *9*, 041040.
- [25] Y.-J. Hao, P. Liu, Y. Feng, X.-M. Ma, E. F. Schwier, M. Arita, S. Kumar, C. Hu, R. Lu, M. Zeng, Y. Wang, Z. Hao, H.-Y. Sun, K. Zhang, J. Mei, N. Ni, L. Wu, K. Shimada, C. Chen, Q. Liu, C. Liu, *Phys. Rev. X* **2019**, *9*, 041038.
- [26] Y. Hu, L. Xu, M. Shi, A. Luo, S. Peng, Z. Y. Wang, J. J. Ying, T. Wu, Z. K. Liu, C. F. Zhang, Y. L. Chen, G. Xu, X.-H. Chen, J.-F. He, *Phys. Rev. B* **2020**, *101*, 161113.
- [27] R. C. Vidal, H. Bentmann, J. I. Facio, T. Heider, P. Kagerer, C. I. Fornari, T. R. F. Peixoto, T. Figgemeier, S. Jung, C. Cacho, B. Büchner, J. van den Brink, C. M. Schneider, L. Plucinski, E. F. Schwier, K. Shimada, M. Richter, A. Isaeva, F. Reinert, *Phys. Rev. Lett.* **2021**, *126*, 176403.
- [28] C. Yan, S. Fernandez-Mulligan, R. Mei, S. H. Lee, N. Protic, R. Fukumori, B. Yan, C. Liu, Z. Mao, S. Yang, *Phys. Rev. B* **2021**, *104*, L041102.
- [29] M.-H. Du, J. Yan, V. R. Cooper, M. Eisenbach, *Adv. Funct. Mater.* **2021**, *31*, 2006516.
- [30] B. Chen, D. Wang, Z. Jiang, B. Zhang, S. Cui, J. Guo, H. Xie, Y. Zhang, M. Naveed, Y. Du, X. Wang, H. Zhang, F. Fei, D. Shen, Z. Sun, F. Song, *Phys. Rev. B* **2021**, *104*, 075134.
- [31] C. Hu, S.-W. Lien, E. Feng, S. Mackey, H.-J. Tien, I. I. Mazin, H. Cao, T.-R. Chang, N. Ni, *Phys. Rev. B* **2021**, *104*, 054422.
- [32] S. Huan, S. Zhang, Z. Jiang, H. Su, H. Wang, X. Zhang, Y. Yang, Z. Liu, X. Wang, N. Yu, Z. Zou, D. Shen, J. Liu, Y. Guo, *Phys. Rev. Lett.* **2021**, *126*, 246601.
- [33] S. H. Lee, D. Graf, L. Min, Y. Zhu, H. Yi, S. Ciocys, Y. Wang, E. S. Choi, R. Basnet, A. Fereidouni, A. Wegner, Y.-F. Zhao, K. Verlinde, J. He, R. Redwing, V. Gopalan, H. O. H. Churchill, A. Lanzara, N. Samarth, C.-Z. Chang, J. Hu, Z. Q. Mao, *Phys. Rev. X* **2021**, *11*, 031032.
- [34] Y. D. Guan, C. H. Yan, S. H. Lee, X. Gui, W. Ning, J. L. Ning, Y. L. Zhu, M. Kothakonda, C. Q. Xu, X. L. Ke, J. W. Sun, W. W. Xie, S. L. Yang, Z. Q. Mao, *Phys. Rev. Mater.* **2022**, *6*, 054203.
- [35] A. M. Shikin, D. A. Estyunin, N. L. Zaitsev, D. Glazkova, I. I. Klimovskikh, S. O. Filnov, A. G. Rybkin, E. F. Schwier, S. Kumar, A. Kimura, N. Mamedov, Z. Aliev, M. B. Babanly, K. Kokh, O. E. Tereshchenko, M. M. Otrokov, E. V. Chulkov, K. A. Zvezdin, A. K. Zvezdin, *Phys. Rev. B* **2021**, *104*, 115168.
- [36] A. Bostwick, T. Ohta, T. Seyller, K. Horn, E. Rotenberg, *Nat. Phys.* **2007**, *3*, 36.
- [37] O. J. Clark, F. Mazzola, J. Feng, V. Sunko, I. Marković, L. Bawden, T. K. Kim, P. D. C. King, M. S. Bahramy, *Phys. Rev. B* **2019**, *99*, 045438.
- [38] Z. El Youbi, S. W. Jung, S. Mukherjee, M. Fanciulli, J. Schusser, O. Heckmann, C. Richter, J. Minár, K. Hricovini, M. D. Watson, C. Cacho, *Phys. Rev. B* **2020**, *101*, 235431.
- [39] Y. Zhang, T.-R. Chang, B. Zhou, Y.-T. Cui, H. Yan, Z. Liu, F. Schmitt, J. Lee, R. Moore, Y. Chen, H. Lin, H.-T. Jeng, S.-K. Mo, Z. Hussain, A. Bansil, Z.-X. Shen, *Nat. Nanotechnol.* **2014**, *9*, 111.
- [40] J. A. Miwa, S. Ulstrup, S. G. Sørensen, M. Dendzik, A. G. Čabo, M. Bianchi, J. V. Lauritsen, P. Hofmann, *Phys. Rev. Lett.* **2015**, *114*, 046802.
- [41] J. Kim, S. S. Baik, S. W. Jung, Y. Sohn, S. H. Ryu, H. J. Choi, B.-J. Yang, K. S. Kim, *Phys. Rev. Lett.* **2017**, *119*, 226801.
- [42] M. Kang, B. Kim, S. H. Ryu, S. W. Jung, J. Kim, L. Moreschini, C. Jozwiak, E. Rotenberg, A. Bostwick, K. S. Kim, *Nano Lett., Nano Lett.* **2017**, *17*, 1610.
- [43] M. Bianchi, P. Hofmann, S. V. Hoffmann, N. C. Jones, Z. Li, J. A. Miwa, S. P. Møller, J. S. Nielsen, H. D. Thomsen, S. Ulstrup, T. Worm, *The European Physical Journal Plus* **2023**, *138*, 132.
- [44] M. Bianchi, R. C. Hatch, J. Mi, B. B. Iversen, P. Hofmann, *Phys. Rev. Lett.* **2011**, *107*, 086802.
- [45] M. Michiardi, I. Aguilera, M. Bianchi, V. E. de Carvalho, L. O. Ladeira, N. G. Teixeira, E. A. Soares, C. Friedrich, S. Blügel, P. Hofmann, *Phys. Rev. B* **2014**, *90*, 075105.
- [46] E. Frantzeskakis, S. V. Ramakutty, N. de Jong, Y. K. Huang, Y. Pan, A. Tytarenko, M. Radovic, N. C. Plumb, M. Shi, A. Varykhalov, A. de Visser, E. van Heumen, M. S. Golden, *Phys. Rev. X* **2017**, *7*, 041041.
- [47] M. Bianchi, R. C. Hatch, Z. Li, P. Hofmann, F. Song, J. Mi, B. B. Iversen, Z. M. Abd El-Fattah, P. Löptien, L. Zhou, A. A. Khajetoorians, J. Wiebe, R. Wiesendanger, J. W. Wells, *ACS Nano* **2012**, *6*, 7009.
- [48] U. A. Schröder, M. Petrović, T. Gerber, A. J. Martínez-Galera, E. Grånäs, M. A. Arman, C. Herbig, J. Schnadt, M. Kralj, J. Knudsen, T. Michely, *2D Mater.* **2016**, *4*, 015013.
- [49] K. Ferfolja, M. Fanetti, S. Gardonio, M. Panighel, I. Piš, S. Nappini, M. Valant, *J. Mater. Chem. C* **2020**, *8*, 11492.

- [50] R. Błaszczyszyn, M. Błaszczyszyn, R. Męclewski, *Surf. Sci.* **1975**, *51*, 396.
- [51] A. Bruix, J. A. Miwa, N. Hauptmann, D. Wegner, S. Ulstrup, S. S. Grønborg, C. E. Sanders, M. Dendzik, A. Grubišić Čabo, M. Bianchi, J. V. Lauritsen, A. A. Khajetoorians, B. Hammer, P. Hofmann, *Phys. Rev. B* **2016**, *93*, 165422.
- [52] P. Zhang, P. Richard, T. Qian, Y.-M. Xu, X. Dai, H. Ding, *Rev. Sci. Instrum.* **2011**, *82*, 043712.